Reflected Path Enhanced Absorbance in an Integrated Photonic Sensor

Jianhao Shen¹, Daniel Donnelly, Swapnajit Chakravarty²
Department of Electro-Optics and Photonics, University of Dayton, 300 College Park, Dayton, OH
USA 45469

ABSTRACT

Evanescent wave sensors in photonic integrated circuits have been demonstrated for gas sensing applications. While some methods rely on the distinctive response of certain polymers for sensing specific gases, absorption spectroscopy identifies any gas uniquely from their unique vibration signatures. Based on the Beer-Lambert principle, the sensitivity of absorption by a gas on chip relies on the length of the sensing region, the optical overlap integral with the analyte gas and the absorption cross-section at the wavelength with the fundamental vibration signature. The overlap of the optical mode with the analyte has been enhanced in photonic devices by combining slot waveguide confinements with photonic crystal slow light effects. While the absorption cross-section is a property of the gas, the length of the sensing region is limited by the available area on a chip and waveguide propagation losses that limit the minimum signal to noise ratio. In this paper, we show that by incorporating reflecting loop mirrors, the absorption path length can be doubled for the same geometric length of the absorption sensing waveguide. Light from a waveguide is split into two paths, each with a slow light photonic crystal waveguide, by a 2×2 multimode interference (MMI) power splitter. Each path is terminated by a loop mirror that causes the light to retrace its path back down the sensing arms thereby doubling the optical path length over which light interacts with the analyte. Results on the enhancement of phase sensitivity and absorbance sensitivity in the interferometric configuration are presented.

Keywords: Michelson interferometer, sensitivity, photonic crystal, waveguide loop mirror, absorbance, slow light

1. INTRODUCTION

Gas/ vapor sensing is a field with wide range of applications including detection of explosives and hazardous chemicals [1], control of industrial processes and emissions [2], breath analysis for medical diagnostics [3], and environmental and atmospheric monitoring [4]. Currently, most gas sensing systems are developed around bulky gas cells and free-space optics based on cavity ring-down spectroscopy (CRDS) [5], tunable diode laser absorption spectroscopy (TDLAS) [6], Fourier transform infrared spectroscopy (FTIR) [7], or photo-acoustic spectroscopy (PAS) [8] methods. Although these systems can provide parts per billion (ppb) and parts per trillion (ppt) sensitivities, they require bulky and expensive optical elements, are very sensitive to beam alignment and have significant size and weight that place constraints on their applications in the field, particularly for airborne or handheld platforms. Infrared absorption spectroscopy is ideally performed in the mid-infrared (mid-IR) molecular fingerprint window from $\lambda=3-12\mu m$ where most molecules have their fundamental absorption signatures. Infrared spectroscopy can selectively identify gases in a mixture/ arbitrary ambient, since they can provide spectroscopic detection and classification. Hence infrared spectroscopy on-chip offers significant advantages over the photonic [9] and electronic nose systems [10] that rely on various polymer matrices for gas selectivity/sensitivity, or graphene sensors with parts per quadrillion (ppq) sensitivities [11], or refractive index dependent long waveguide interferometers [12] or fixed wavelength narrow bandwidth slow light waveguide sensors [13] with ~100ppb sensitivities, that are all affected by cross-talk from gas/vapor mixtures and their relative concentrations in the mixture.

2. DESIGN

2.1 Michelson Interferometer Sensor Structure

During the past decade, architectures for on-chip laser absorption sensing [13-16] have been proposed and developed to achieve high gas sensing sensitivity on-chip. The Beer-Lambert absorption law given in Eq. 1 is the fundamental equation that governs the optical absorbance of gases at wavelengths corresponding to their molecular vibration signature

1 shenj5@udayton.edu;

2 schakravarty1@udayton.edu; phone 1 937 229-2747;

frequencies. The exponential term in Eq. 1 indicates a dependence on αL where α is the absorption coefficient per unit length and L is the effective optical path length over which the gas or analyte interacts with the optical mode.

$$I = I_0 \exp[-\alpha L] \tag{1}$$

In benchtop systems, effective path length L can reach kilometers in some instances by reflecting the wavelengths over which gas absorption is expected, between highly reflective polished mirrors, albeit over an extremely narrow range of wavelength. However, on the chip level, where chip dimensions are a centimeter in length or even smaller, long waveguide lengths are usually achieved by spiraling low loss strip waveguides or by using slow wave reduction of the optical path length in straight photonic crystal waveguides. In this paper, we demonstrate an interferometric device to enhance the analyte absorption. In a typical balanced Mach-Zehnder interferometer, the input light splits into two waveguides of equal length L using a power splitter, which can be either a Y-junction splitter or a multimode interference (MMI) splitter, denoted by MMI_A in Figure 1. When the two balanced arms combine at the output power combiner MMI_B, the net power absorption at a wavelength corresponding to the absorption wavelength of the analyte is the same as that for a straight waveguide of the same length L. If the output arms of MMI_B are connected in the form of a loop waveguide mirror to reflect the light back to the interferometer arms, light propagates an additional distance L before exiting to the output of MMI_A as shown schematically in Figure 1. The total absorption path length is thus 2L for the same geometric path length L of the interferometer arms. Since both arms of the balanced interferometer are exposed to the same analyte gas, the reflected light at the power combiner MMI_B in the balanced interferometer configuration exits with maximum amplitude to the output port of MMIA, reduced only by the absorbance of the analyte gas or vapor. In slow light structures, a modified form of the Beer-Lambert absorption law [17, 18] follows Eq. 2 where

$$I = I_0 \exp[-\gamma \alpha L] \tag{2}$$

where I_0 is the incident intensity, α is the absorption coefficient of the medium, L is the interaction length, and γ is the medium-specific absorption factor determined by dispersion enhanced light-matter interaction. In conventional free-space systems, $\gamma = 1$; in slow light systems, γ is given by Eq. 3:

$$\gamma = f \times \frac{(c/n)}{v_g} \tag{3}$$

where c is the velocity of light in free space, v_g is the group velocity in medium of effective index n, and f is the fill factor denoting relative fraction of optical field residing in the analyte medium. Equation 3 shows that slow light propagation (small v_g) significantly enhances absorption. Furthermore, the greater the electric field overlap with analyte, the greater the effective absorption by the medium. The effective absorption equation in our slow wave enhanced reflected path on-chip absorbance sensor is given by Eq 4 as:

$$I = I_0 \exp\left[-f \times \frac{(c/n)}{v_g} \alpha(2L)\right] \tag{4}$$

where the factor 2 in the exponent indicates the higher absorbance per unit geometric length in the reflected path configuration. We experimentally establish the enhanced absorbance and enhanced phase sensitivity in the Michelson configuration with the reflective loop mirror, and Mach-Zehnder configuration without a reflective loop waveguide mirror.

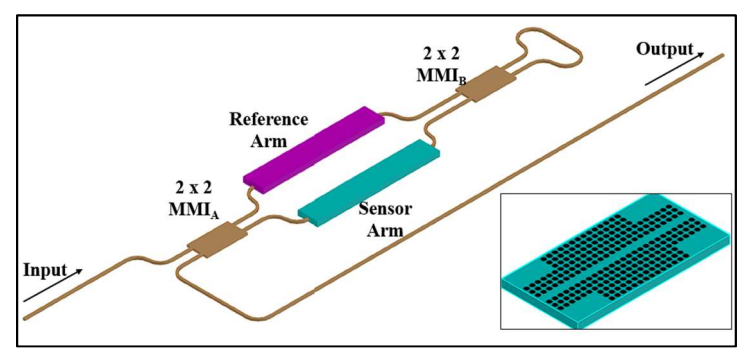


Figure 1. Schematic of Michelson interferometer chem-bio sensor design with symmetric 2D PCW arms in silicon. Asymmetry results from cladding the reference arm with silicon dioxide and the signal arm with the analyte liquid or gas/vapor.

Figure 2(a) shows a schematic of the slow light path enhanced reflected path unbalanced interferometer sensor (Michelson configuration). A two-dimensional photonic crystal waveguide (2D-PCW) with different lengths 5 µm and 20 µm is fabricated on the reference arm and the signal arm respectively. We consider a W1 PCW (with lattice period a and a single missing row of air holes in the Γ – K direction of propagation. The PCW is adiabatically tapered from the width W1 $(=1*\operatorname{sqrt}(3)*a)$ to a width W1.08 $(=1.08*\operatorname{sqrt}(3)*a)$ over 16 lattice periods to enhance coupling efficiencies from the access 500nm wide strip waveguides into the slow light waveguide at the higher group indices near the photonic stop band edge. The reference arm is covered with a 100nm thick silicon dioxide top cladding which also fills the corresponding PC air holes. The silicon dioxide is completely removed from the signal arm as also the PC air holes so that the air holes on the signal arm are completely exposed to analytes. On both arms, the PC air holes are etched in 220nm silicon, with a=395nm, and air holes radius r given by r/a=0.275. A 2×2 MMI splits the input lights into the two interferometer arms. The interferometer arms meet at a second 2×2 MMI whose output arms are connected to each other via a waveguide loop mirror. Figure 2(b) shows a top view microscope image of the slow wave Michelson interferometer (MI) sensor device. Figure 2(c) shows the SEM image in top view of the 2D PCW etched air holes on the signal arm, noting that on the reference arm, the PCW is covered with silicon dioxide. Devices were fabricated using standard process development kit (PDK) components for grating couplers at AIM Photonics. The 2×2 MMI was designed to achieve 50:50 splitting between the two output arms.

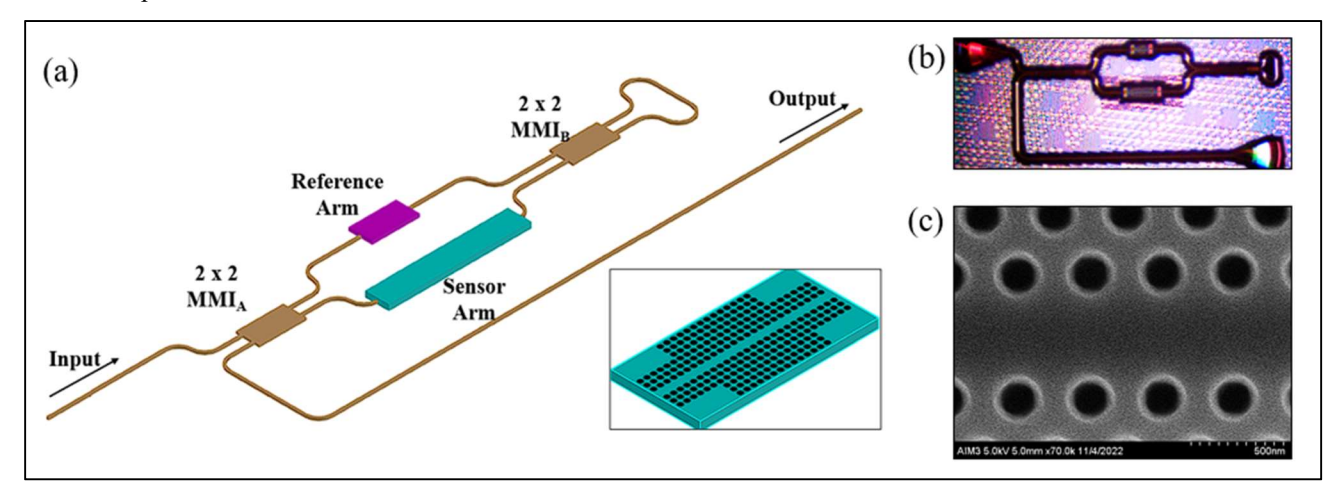


Figure 2. (a) Schematic of Michelson unbalanced interferometer chem-bio sensor design; (b) The microscope image of the Michelson interferometer sensor fabricated on chip; (c) Scanning electron microscope (SEM) image of the etched holes on the photonic crystal structure.

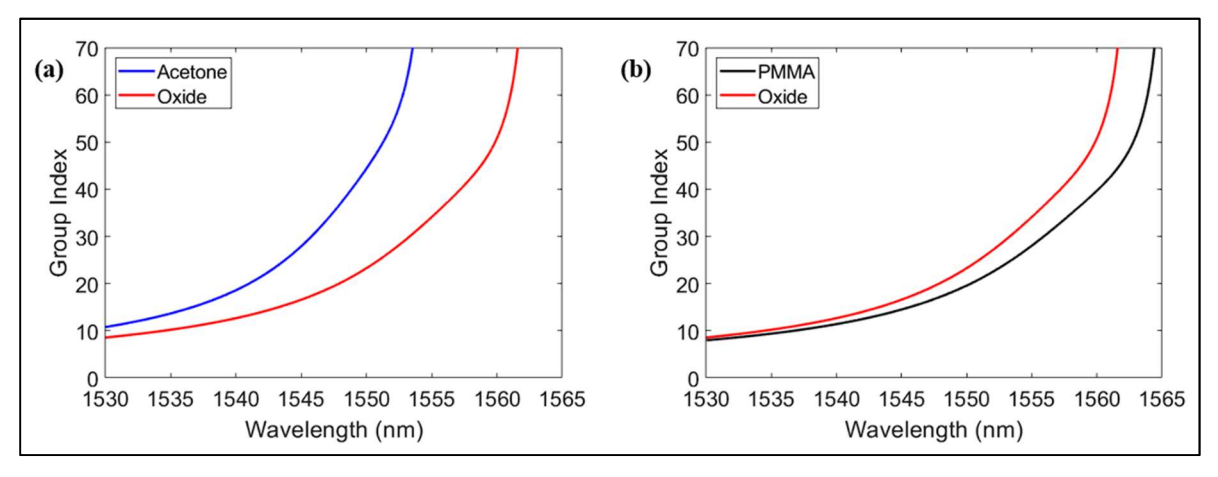


Figure 3. Simulated group index profile versus wavelength of 2DPCW single device with (a) acetone cladding and silicon dioxide cladding; (b) PMMA cladding and silicon dioxide cladding respectively.

Figure 3 shows the change of the simulated group index with increasing wavelength of the 2DPCW configuration with lattice constant of 395nm with acetone cladding, silicon dioxide cladding, and PMMA cladding separately. The group index increases with wavelength as one approaches the PCW stop band edge. The band edge moves to longer wavelengths for the same PCW device with increasing refractive index of the top cladding/ analyte and thus the band edge with silicon dioxide top cladding is in between that of acetone and PMMA.

2.2 Theoretical Phase Sensitivity

In sensing application, the bulk spectral sensitivity, simply defined as the wavelength shift per unit change in analyte refractive index with units of nanometers/RIU (RIU=refractive index unit), is typically used for microcavity resonator devices. For interferometer sensors, the theoretical phase changes induced in the guided mode on the sensing arms is given as:

$$\Delta \psi_S = \frac{2\pi}{\lambda} \Delta N_S L \tag{5}$$

where, λ is the wavelength of light, ΔN_S is the change in the effective index of the guided mode in contact with the analyte, and L is the length of the sensing arm. In the case of the Michelson interferometer, the effective optical path length (L_{MI}) is twice the effective path length (L_{MZI}) for a Mach-Zehnder interferometer. Hence the effective optical phase shift is twice in the MI versus the MZI for the same geometric path length. The interferometer phase sensitivity S_{phase} is given as:

$$S_{phase} = \frac{S_{spectral}}{\Delta \lambda \times L_S} \times 2\pi \tag{6}$$

Where $S_{spectral}$ is the bulk spectral sensitivity calculated by the ratio of the wavelength shift on the same peak and the corresponding refractive index change.

3. RESULTS

Bulk sensitivity measurements are first performed to determine the spectral response of the slow light Michelson interferometer sensor to changes in the signal arm analyte refractive index changes. Light is coupled into the grating couplers from a tunable laser (Santec TSL-710) and the output optical signal is measured with a synchronized power meter. The experimental transmission spectra for individual 2D PCW devices covered with silicon dioxide and separately with acetone are shown in Figure 4. The blue curve is the spectrum of the 2D PCW covered by acetone on the top and silicon dioxide on the bottom. The red curve shows the spectrum of the 2D PCW covered with silicon dioxide both on top and bottom. From Fig. 4, we can identify three regions highlighted with three different colors. For the light with wavelengths inside the red region, both signal and reference arms are forbidden for light propagation, leading to no interferences at all. When the wavelength goes down to the yellow region, the reference arm with silicon dioxide top cladding allows propagation, yet propagation on the sensor (signal) arm is still forbidden. In the green region, light can propagate on both arms of the interferometer. The green bounded region of wavelengths is the working wavelength range for the slow wave interferometer sensor. The band edge is at $\lambda \sim 1548$ nm for acetone top cladding and at $\lambda \sim 1571$ nm for oxide top cladding.

The analyte is introduced with a pipette over the signal arm. The wavelength sweeps in our measurements across the entire C- and L-bands in our setup can be done in 1 second which ensures that any analyte does not evaporate during the time span of the measurements. In the literature, various bulk sensitivity measurements are done by varying concentrations of salt water and sugar-water solutions, however such sample introductions can potentially compromise the chip from any further measurements due to residues that can remain inside the nanostructured holes. Hence acetone (n=1.3586) and isopropyl alcohol (IPA, n=1.3772) were selected to experimentally determine the sensitivity characteristics of the device.

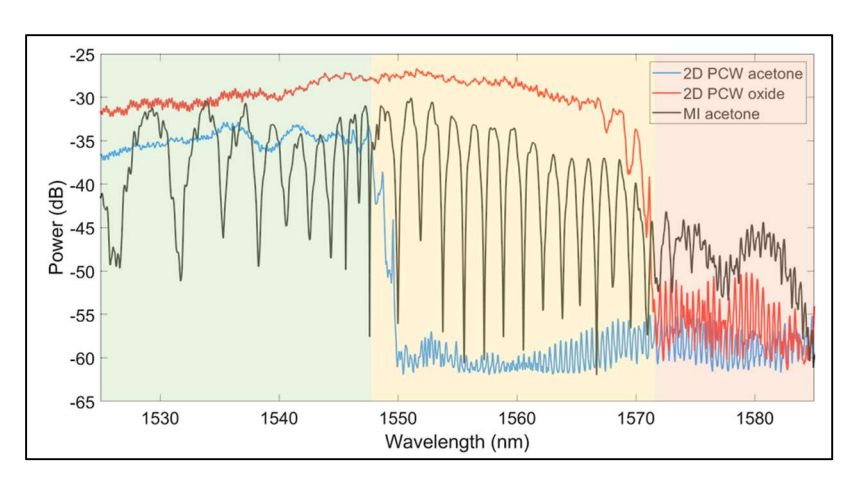


Figure 4. Transmission spectra of the Michelson interferometer sensor covered with acetone, and individual 2D PCW devices covered with acetone and silicon dioxide respectively as on the signal arm and reference arm respectively. Green shaded region indicates the range of wavelength over which light propagates in both interferometer arms. In the yellow shaded wavelengths, light propagates only in the oxide clad reference arm. In the red shaded region, the transmission is cut off from both arms by the individual photonic stop bands.

The bulk sensitivity is estimated from the wavelength shift of the interference fringes at different analyte refractive indices. The bulk sensitivity from the experiment is comparable to that of conventional silicon MZI sensors but in more than an order of magnitude shorter dimensions. Figure 5 plots the fringe spacing for the experimentally observed interference fringes for the device in Fig. 2. The fringe spacing, defined as the wavelength separation between adjacent interference fringes, decreases as the transmission approaches the band edge where light propagates with higher group index.

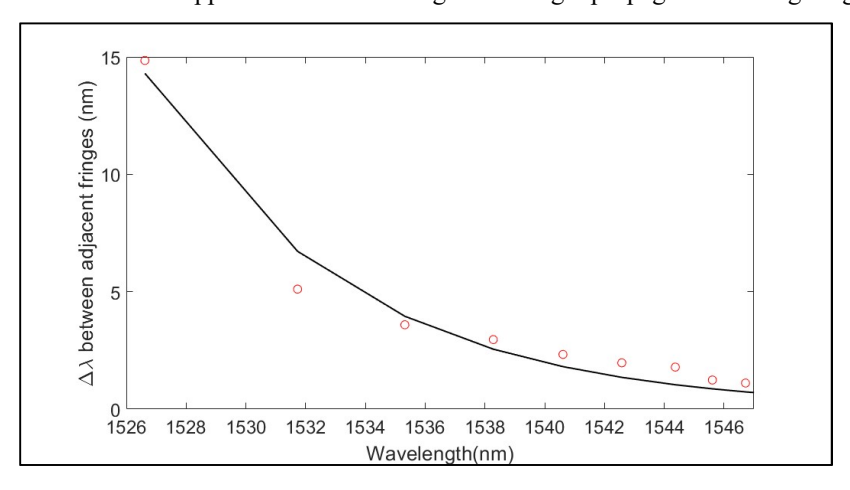


Figure 5. Fringe Spacing versus wavelength for the observed interference fringes

The phase sensitivity was calculated from Eq. (4) based on the measurements and plotted in Figure 6. From the experimental values, the phase sensitivity at $\lambda \sim 1547$ nm is $\sim 300,000$ rad/RIU-cm. Compared with $\sim 84,000$ rad/RIU-cm for MZI in ref. [19], our MI could reach almost four times the phase sensitivity. Transmission simulations for the oxide clad photonic crystal waveguide arm indicates that in the fabricated devices, the experimental photonic stop band edge is red shifted by ~ 7 nm thus indicating that the fabricated hole dimensions are smaller than design. In contrast, on the analyte clad arm, the experimental transmission band edge is blue shifted by ~ 5 nm compared to simulations indicating an incomplete filling of the air holes by the analyte acetone. If acetone completely filled the air holes, the bulk sensitivity experimentally observed would be higher leading to a higher phase sensitivity than experimentally observed.

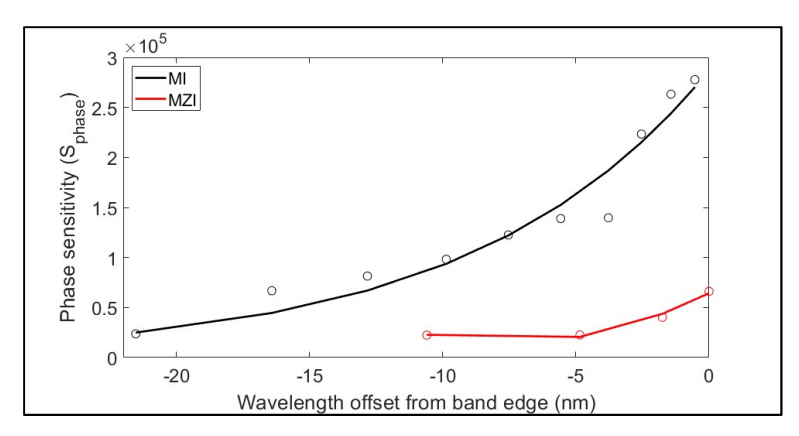


Figure 6. Fitted phase sensitivity for the Michelson interferometer and Mach-Zehnder interferometer configuration

A similar theoretical analysis on the enhanced absorbance of our reflected path interferometer in Fig. 1 was performed to compare with the absorbance of the straight waveguide of the same geometrical path length. We considered an interferometer with equal slow light 2D PCW geometric path lengths ($80\mu m$) for the reference arm and the signal arm as the straight 2D PC waveguide. The reference arm is covered with silicon dioxide, while the signal arm is exposed to the analyte, PMMA. From Figure 3(b), we observe at the wavelength 1553nm, the group index changes from 24.2 to 29.3 when the top cladding in the 2DPCWs changes from PMMA (n=1.4717, k=0.00003) [20] to silicon dioxide (n=1.445, k=0.00002) [21]. By inserting the values of n_g into Eq. (4) for equal arm length in the two paths of the interferometer, we estimated that the reduction in power is 2dB for an $80\mu m$ -long 2DPC slow light waveguide, in the Mach-Zehnder configuration when the top cladding of the signal arm changes from silicon dioxide to PMMA. In contrast, the reduction in power is 4dB when the light is reflected back to the interferometer arms by the waveguide loop mirror in the Michelson configuration. Experiments are in progress to validate the reflected path enhanced absorption principle with gases. Figure 3(b) also shows that the absorbance change increases for the wavelengths close to the transmission band edge. Future designs can incorporate high group index and wide optical bandwidth 2DPCW geometries in the reflected path Michelson interferometer configuration for wider bandwidth absorbance sensing.

4. CONCLUSION

In summary, we demonstrated an on-chip reflected path slow wave interferometer sensor with enhanced phase sensitivity and enhanced absorbance sensitivity compared to an equivalent Mach Zehnder interferometer sensor. Our experimental measurements show nearly 4× enhancement of the phase sensitivity of reflected path interferometer sensors in Michelson configuration compared to the equivalent Mach-Zehnder with the same geometric path length difference. Numerical analysis also shows a 2× enhancement in the power attenuation upon absorbance in the reflected path enhanced sensors compared to the straight slow light waveguides of equal geometric length.

5. ACKNOWLEDGEMENTS

The authors thank the National Science Foundation (NSF) grant #2210707 for supporting this work and AIM Photonics for foundry fabrication under DCL NSF 21-015. D.D. also acknowledges support from the University of Dayton Summer Undergraduate Research Experience (SURE) fellowship. J.S. has been supported in part by the University of Dayton Office for Graduate Academic Affairs through the Graduate Student Summer Fellowship Program.

6. REFERENCE

- [1] A. Raupke, A. Palma-Cando, E. Shkura, P. Teckhausen, A. Polywka, P. Gorrn, U. Scherf, T. Riedl, "Highly sensitive gas-phase explosive detection by luminescent microporous polymer networks" Nat. Scientific Rep. 6, 29118 (2016)
- [2] I.M. Perez de Vargas-Sansalvadoe, C. Fay, T. Phelan, M.D. Fernandez-Ramos, L. F. Capitan-Vallvey, D. Diamond, F. Benito-Lopez, "A new light emitting diode-light emitting diode portable carbon dioxide gas sensor based on an interchangeable membrane system for industrial applications", Anal. Chim. Acta 699 (2), 216 (2011)

- [3] C. Kim, I. S. Raja, J-M. Lee, J.H. Lee, M.S. Kang, S.H. Lee, J-W. Oh, D-W. Han, "Recent Trends in Exhaled Breath Diagnosis Using an Artificial Olfactory System", Biosensors 11 (9), 337 (2021)
- [4] S. Dhall, B. R. Mehta, A. K. Tyagi, K. Sood, "A review on environmental gas sensors: Materials and technologies", Sensors International 2, 100116 (2021)
- [5] M. J. Thorpe, K. D. Moll, R. J. Jones, B. Safdi, J. Ye, "Broadband Cavity ringdown spectroscopy for sensitive and rapid molecular detection," Science 311, 1595 (2006)
- [6] P. Werle, "Tunable diode laser absorption spectroscopy: recent findings and novel approaches", Infrared Phys. And Tech. 37, 59 (1996)
- [7] C. Smith, "Fundamentals of Fourier Transform Infrared Spectroscopy", ISBN 9781420069297, CRC Press, 2nd Edition (2011)
- [8] K. H. Michaelian, "Photoacoustic Infrared Spectroscopy", Series: Chemical Analysis v. 159, ISBN: 0471134775: 9780471134770, Hoboken, N.J.: Wiley-Interscience (2003)
- [9] L. Laplatine, M. Fournier, N. Gaignebet, Y. Hou, R. Mathey, C. Herrier, J. Liu, D. Descloux, B. Gautheron, T. Livache, "Silicon photonic olfactory sensor based on an array of 64 biofunctionalized Mach-Zehnder interferometers" Opt. Exp. 30 (19), 33955 (2022)
- [10] A. D. Wilson, "Application of Electronic-Nose Technologies and VOC-Biomarkers for the Noninvasive Early Diagnosis of Gastrointestinal Diseases", Sensors 18 (8), 2613 (2018)
- [11] G. Chen, T. M. Paronyan, A.R. Harutyunyan, "Sub-ppt gas detection with pristine graphene", Appl. Phys. Lett. 101, 053119 (2012)
- [12] G. Antonacci, J. Goyvaerts, H. Zhao, B. Baumgartner, B. Lendl, R. Baets, "Ultra-sensitive refractive index gas sensor with functionalized silicon nitride photonic circuits", APL Photon. 5, 081301 (2020)
- [13] Y. Zou, S. Chakravarty, P. Wray, R. T. Chen, "Mid-Infrared Holey and Slotted Photonic Crystal Waveguides in Silicon-on-Sapphire for Chemical Warfare Simulant Detection," Sensors and Actuators B 221, 1094 (2015)
- [14] Y. Zou, S. Chakravarty, P. Wray, R. T. Chen, "Mid-Infrared Holey and Slotted Photonic Crystal Waveguides in Silicon-on-Sapphire for Chemical Warfare Simulant Detection," Sensors and Actuators B 221, 1094 (2015)
- [15] J. Midkiff, S. Chakravarty, K. Yoo, A. Rostamian, R. T. Chen, "Monolithic integration of quantum cascade laser, quantum cascade detector, and subwavelength waveguides for mid-infrared integrated gas sensing" Proceedings of the SPIE 109261V (2019)
- [16] M. Vlk, A. Datta, S. Alberti, H.D. Yallew, V. Mittal, G.S. Murugan, J. Jagerska, "Extraordinary evanescent field confinement waveguide sensor for mid-infrared trace gas spectroscopy", Nature: Light Science and Applications 10, 26 (2021)
- [17] N. A. Mortensen and S. S. Xiao, "Slow-light enhancement of Beer-Lambert-Bouguer absorption", Appl. Phys. Lett. 90, 141108 (2007)
- [18] W-C. Lai, S. Chakravarty, X. Wang, C. Lin, R.T. Chen, "Photonic Crystal Slot Waveguide Absorption Spectrometer for On-Chip Near-Infrared Spectroscopy of Xylene in Water", Appl. Phys. Lett. 98 (2), 023304 (2011)
- [19] K. Qin, S. Hu, S. T. Retterer, I. I. Kravchenko, S. M. Weiss, "Slow light Mach–Zehnder interferometer as label-free biosensor with scalable sensitivity", Optics letters 41(4), 753 (2016)
- [20] X. Zhang, J. Qiu, J. Zhao, X. Li, L. Liu, "Complex refractive indices measurements of polymers in infrared bands", Journal of Quantitative Spectroscopy and Radiative Transfer 252,107063 (2020)
- [21] J. Kischkat, S. Peters, B. Gruska, M. Semtsiv, M. Chashnikova, M. Klinkmüller, O. Fedosenko, S. Machulik, A. Aleksandrova, G. Monastyrskyi, Y. Flores, W. T. Masselink "Mid-infrared optical properties of thin films of aluminum oxide, titanium dioxide, silicon dioxide, aluminum nitride, and silicon nitride", Applied optics 51(28), 6789 (2012)